Mixed convective heat transfer from a permeable square cylinder: A lattice Boltzmann analysis

CrossMark

T.R. Vijaybabu, K. Anirudh, S. Dhinakaran *

The Centre for Fluid Dynamics, Discipline of Mechanical Engineering, Indian Institute of Technology Indore, Khandwa Road, Simrol, Indore, Madhya Pradesh 453 552, India

ABSTRACT

The flow and mixed convection heat transfer from a two-dimensional porous square cylinder under the influence of aiding buoyancy in an infinite stream are analysed employing a mesoscopic approach. Reynolds number (Re) and Darcy number (Da) considered in this study vary from 2 to 40 and 10^{-6} to 10^{-2}, respectively. The flow and heat transfer characteristics at the Prandtl number value of 0.71 (air) is compared for three different values of Richardson number (Ri) i.e. 0, 0.5 and 1. The numerical experiments in this study are carried out by using Lattice Boltzmann technique with two distribution functions. The BGK collision operator with Darcy-Forchheimer and Boussinesq force terms are added to the LB collision equation. Mach number annealing process is also carried out to accelerate the simulations. Flow and heat transfer characteristics are found to be a function of non-dimensional permeability (Da), buoyancy condition and Reynolds number. It is observed that a monotonous reduction occurs in the wake length and drag coefficient values at higher permeability levels. Whereas, aiding buoyancy depicts a pronounced reduction in wake length and an increment in drag coefficient values. The heat transfer enhancement ratio for all surfaces of the cylinder and mean Nusselt number were calculated to compare the thermal behaviour at various Ri and Da values. A significant augmentation in heat dissipation is reported for increasing values of Ri and/or Da. The percentage increment in mean Nusselt number at $Re = 40$, $Da = 10^{-2}$ is found to be 18% and 34% for $Ri = 0.5$ and 1, respectively with reference to the forced convection case. Also, heat transfer is maximum at $Da = 10^{-2}$ and $Ri = 1$ for the flow regime considered in this study. Correlations for mean Nusselt number, valid for the range of parameters considered in the present study, are also provided. The key results obtained from this study can be helpful for further research in different realms of engineering sciences, especially thermal engineering, aided by porous media modeling approach.

© 2017 Elsevier Ltd. All rights reserved.

1. Introduction

Diverse engineering applications can be modeled or approximated as transport through porous media. Such instances can be found in packed bed heat exchangers, drying technology, catalytic reactors, thermal insulation, petroleum industries and electronic cooling. These modeling techniques can be an invaluable tool for the designers in different fields of engineering. Transport phenomena in porous media has been predominantly used in the field of geothermal engineering such as underground flow and filtration. However, more recently, attention is being paid for the application of porous media theory in thermal engineering, specifically for the purpose of heat transfer enhancement in compact devices. This occurrence accounts due to the inherent property of porous bodies,

providing more surface area for heat dissipation in the same volume compared to solid bodies. A vast amount of books and articles, depicting typical case studies for application and numerical tools based on porous medium, are available in the literature [1–11]. Additionally, recent research works related to porous medium [12,13] have shown its ability on heat transfer magnification. Another prime advantage with the porous media modeling technique is that, it can be used to simplify a complex system with numerous elements into a single porous object. This empowers the engineer to discover experimentally unapproachable problems with significant computational economy. A relevant example would be of a nuclear reactor core, wherein the arrangement of fuel and control rods resemble a porous square system, as shown in Fig. 1. Such arrangements can be tuned to receive required flow and heat transfer characteristics. Thus, numerous research attempts are in progress to capture enhancement in the heat transfer performance by using porous media.

* Corresponding author.
E-mail address: ssdhinakar@gmail.com (S. Dhinakaran).

Nomenclature

Notations

AB	front face of the cylinder
BC	right face of the cylinder
CD	rear face of the cylinder
DA	left face of the cylinder
C_D	coefficient of drag, $\frac{F_D}{0.5\rho v_0^2}$
c_F	non-dimensional Forchheimer form-drag coefficient
c_s	speed of sound, [m s^{-1}]
Da	Darcy number, $\frac{K}{H^2}$
d_p	particle diameter, [m]
e_i	discrete lattice velocity in direction i, $\frac{\delta x_i}{\delta t}$
F_b	Boussinesq force term, [N]
f_i	particle density distribution function along i^{th} link direction
f_i^{eq}	equilibrium distribution function of density along i^{th} link direction
F	body force due to the presence of the porous medium, [N]
F_i	total force term due to porous medium, [N]
g	gravitational acceleration, [m s^{-2}]
g_i^{eq}	equilibrium distribution function of temperature along i^{th} link direction
g_i	temperature distribution function along i^{th} link direction
G	body force due to gravity, [N]
H	height of the cylinder, [m]
K	permeability of the material, [m^2]
L_D	downstream length, [m]
L_U	upstream length, [m]
Ma	Mach number, $\frac{v}{c_s}$
N	number of lattices on the cylinder
Nu	local Nusselt number, $\frac{\partial\theta}{\partial n}$
Pr	Prandtl number, $\frac{v}{\alpha}$
Re	Reynolds number, $\frac{v_\infty H}{v}$

Ri	Richardson number, $\frac{g\beta\triangle\theta H}{v_0^2}$
T	dimensional temperature, [°C]
u^*	dimensional x-component velocity, [m s^{-1}]
v^*	dimensional y-component, [m s^{-1}]
u	non-dimensional x-component velocity, [m s^{-1}]
v	non-dimensional y-component velocity, [m s^{-1}]
V	auxiliary velocity, [m s^{-1}]
w_i	weighing factor in direction i
x^*, y^*	dimensional horizontal & vertical coordinate
x, y	non-dimensional horizontal & vertical coordinate

Greek symbols

ρ	fluid density, [kg m^{-3}]
τ	dimensionless relaxation time for density
τ'	dimensionless relaxation time for temperature
$\triangle x$	lattice space
$\triangle t$	time step
v	fluid kinematic viscosity, [m^2 s^{-1}]
ϕ	porosity
θ	dimensionless temperature, $\frac{T-T_\infty}{T_w-T_\infty}$
β	thermal expansion coefficient, [°C^{-1}]
τ_t	non-dimensional time, $\frac{tv_\infty}{H}$

Subscripts

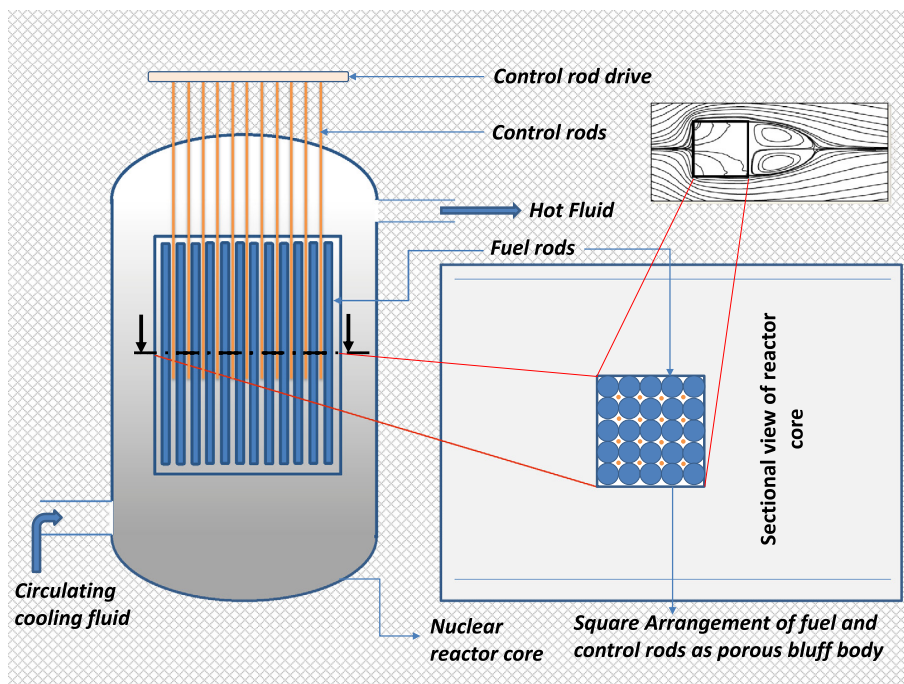|	
∞	far field value
o	inlet value
M	mean value
i	lattice link direction
w	wall
f	front face
r	rear face
s1	left face
s2	right face

Fig. 1. An example of a scenario of flow around and through square shaped porous body - Fuel and control rods of a nuclear reactor mimic this situation.

Porous bluff body research is also in vogue amongst researchers due to primarily two main reasons: (a) Its simplicity in terms of studying flow and heat transfer from it; (b) Representative modeling of staggered real-life complex structures, which are numerically expensive to model. These porous bodies, of different shapes and at permeability levels, can seriously affect the flow phenomena *i.e.* delay in occurrence and later, suppression of wake and vortex shedding. And they can also provide significant augmentation in thermal dissipation [14–19]. At very low permeability levels (i.e. $Da \leq 10^{-6}$), the porous bluff body mimics a solid body and the heat transfer performance is same as that of an impermeable cylinder. Increase in permeability levels, allows fluid to flow through the permeable cylinder, resulting in increased heat transfer rate. Most of the studies [18–23] have concentrated on forced convective heat transfer from a permeable body rather than practically occurring mixed convection. Consequently, it becomes necessary to look into the conjugative effects of mixed convection heat transfer phenomena and porous media. Hwang and Chao [24] investigated the effects of permeability on laminar mixed convection in a fully developed square channel filled with porous medium. They revealed that the nonuniform wall temperature distribution greatly influences the flow and heat transfer characteristics. Bae et al. [25] studied the mixed convection heat transfer in a channel containing multiple porous blocks heated from bottom. They used Brinkman-Forchheimer-extended Darcy model and two-equation energy model to characterize the flow and temperature inside the porous blocks in which higher heat transfer performances is reported. With reference to the experiments, Chou et al. [26] investigated the fully developed non-Darcian mixed convection in horizontal packed sphere channels experimentally. Their analysis has shown that the buoyancy effect significantly affects the flow structure and heat transfer rate at low Peclet number. Kurtbas and Celik [27] experimentally investigated the mixed convection flow through a horizontal rectangular channel with open-cell metal foams of different pore densities. It has been revealed that the buoyancy driven secondary flow and higher pore density supplements the augmentation of the mean Nusselt number. From the aforementioned studies, it can be seen that higher heat transfer rates could be attained by using porous media under the influence of buoyancy. Mixed convection flow through a porous medium has been applicable to electronic component cooling system, light emitting diode (LED) backlight module system, LED street lamp cooling equipment, heat exchangers, thermal insulations and drying process [28]. A thorough knowledge of the flow and heat transfer parameters like drag, lift, wake length and Nusselt number is crucial to design aforementioned applications.

On the parallel lines of the above discussion, work has also been done on mixed convection from porous bluff bodies for different operating conditions. It is well-known that a porous cylinder at lower values of permeability, behaves like a solid one. Hence, mixed convection from such a porous cylinder would obviously exhibit heat transfer trends similar to that from a solid cylinder. Such an instance can be visualised from the numerical study performed by Sharma et al. [29], wherein they showed the influence of aiding buoyancy on a 2D solid square cylinder in vertical unconfined configuration. They have calculated the local and average Nusselt number for Reynolds number and Richardson number ranges from 1–40 and 0–1, respectively. It was found that the drag coefficient increases at higher values of *Ri*, compared to the forced convection case. It was further emphasised that the average Nusselt number is weakly dependent on the cross-buoyancy condition in steady regime for an unconfined flow domain. They have also formulated simple correlations for the wake length and average Nusselt number for the range of conditions embraced. Wu and Wang [28] numerically investigated mixed convection effect on a porous square cylinder with the heated cylinder bottom for cylinder to channel ratio 0.1, 0.3 and 0.5 at *Re* = 250. Their results depict that although at higher channel to cylinder ratios (B/H = 0.3 & B/H = 0.5) the buoyancy effect is not clear, it still has rich heat transfer characteristics. However, at B/H = 0.1 the laminar flow motion is only noticeable near the porous square cylinder and there is not much effect on cylinder wall. Guerroudj and Kahalerras [30] numerically examined the influence of porous block shape and height on a partially heated lower plate under different cross-flow buoyancy conditions. Their results show that the intensity of cross-flow buoyancy and Reynolds number increases the strength of vorticity irrespective to the size and shape of porous body. Furthermore, it has been reported that the heat transfer rate is maximum with buoyancy parameter (i.e. *Ri*) and it is found to be high for triangular shaped cylinder even at low permeability values. Later, Guerroudj and Kahalerras [31] studied the flow and heat transfer in an inclined channel provided with heated porous block on its lower plate. They have found that maximum and minimum heat dissipation occurs when channel angle approaches $+90^\circ$ (aiding buoyancy) and -90° (opposing buoyancy), respectively. However, an optimum angle for maximum Nusselt number has been reported as 30° for low permeability values. It can be understood from the above discussion that mixed convection heat transfer from an isolated porous square cylinder has not been studied yet, although studies on forced convection exist. Moreover, there is no information available in the literature on the drag and Nusselt number of the porous square cylinder which is important to design heat exchangers, LED backlight module cooling system under the mixed convective conditions.

Complex applications usually require appropriate and, in most cases, more sophisticated mathematical and numerical modeling. Since the advent of Boltzmann method for solving transport equations, LBM has shown its effectiveness against conventional approaches, especially while dealing with complex flow domain, flow through porous media and multiphase flow. In 1988, LBM was introduced by McNamara and Zanetti to overcome the drawbacks of the lattice gas cellular automata [32]. Since then researchers have been started smearing this mesoscopic technique in various domains. LBM can be employed in wide range of applications in the field of Micro Electro Mechanical Systems (MEMS) and Nano Electro Mechanical Systems (NEMS) [33]. Also, compared to the convectional numerical methods LBM is more appropriate for parallel processing and it solves multiphase flows easily. Recent research articles [34–41] indicate that the flow modeling for non-Newtonian fluids and nano-fluids is quite simple which carries an addition of external force term with the LB flow evolution equation. Numerical simulations of unsteady flow around a square cylinder located between two parallel plates using FVM and LBM were investigated by Breuer et al. [42]. The vortex shedding phenomenon behind a porous square cylinder is probed by Babu and Narasimhan [43] at Re = 100 and 200. They have employed D2Q9i lattice model in which entire collision equation with force term is written in terms of pressure. The main advantage of this approach is Navier-Stokes equations can be recovered from the LB equations within $O(Ma^2)$ [43]. Also, a force term F_i which accounts for drag effects due to the presence of porous medium is added explicitly with the collision equation to characterize the flow through the porous medium. Most of the other studies [44–49] imply that employing LBM for porous medium is quite simple and efficient. By considering these advantages, we have applied LB technique in our study. The objective of the present study is, therefore to investigate in detail the flow and thermal field around an isolated porous square cylinder and to explore the influence of permeability and aiding buoyancy on heat transfer from it. A LB model for the flow through porous media proposed by Guo and Zhao [45] is included.

2. Mathematical formulation

2.1. Problem definition

Consider a square cylinder of height H, maintained at a constant temperature T_w, and exposed to a constant free stream velocity v_∞ (flowing in the positive y-direction) which is at an ambient temperature T_∞ as shown in Fig. 2. Although the objective is to simulate the flow and mixed convective heat transfer around the cylinder when it is placed in an infinite stream, for making computationally feasible, the domain was limited to rectangular configuration. The following assumptions were made in order to make the problem amenable to numerical simulations:

- The problem under consideration is steady, laminar, two-dimensional, incompressible and the fluid is Newtonian. The fluid flows around and through an isotropic, homogenous porous matrix with constant porosity and permeability.
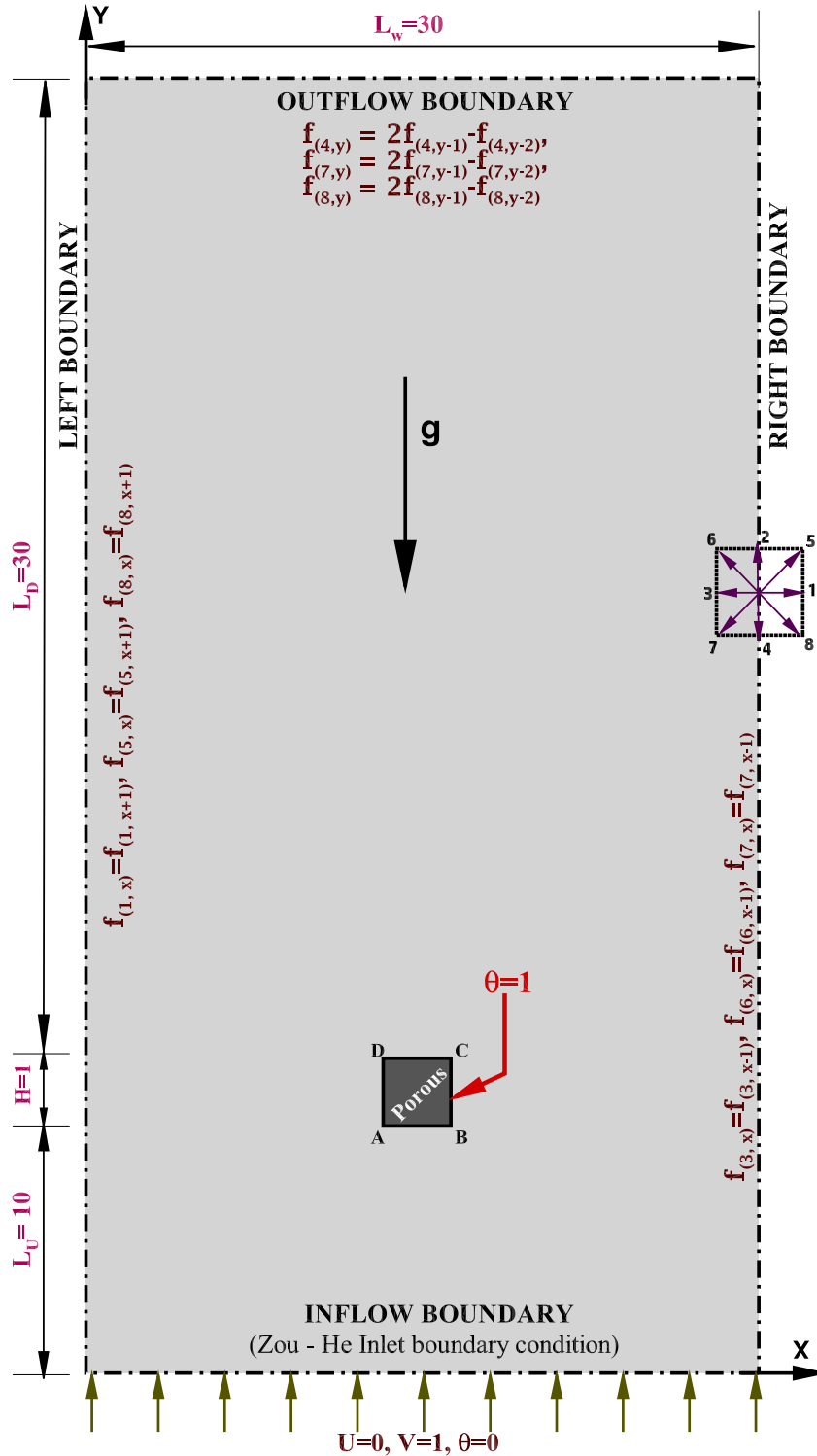

Fig. 2. Computational domain used in the analysis of mixed convection flow and heat transfer from a porous square cylinder.

- All the fluid properties are considered to be constant and the body forces are negligible, except for the body force terms in the collision equation (Boussinesq approximation in y direction) in this study.
- There is no heat generation in the porous cylinder and viscous dissipation is negligible. Further, the fluid phase temperature is equal to that of the porous phase (i.e. Local Thermal Equilibrium - LTE). This boundary condition should not be considered for rapid cooling or heating process or problems with significant temperature variation across the porous media [50]. However, the temperature difference between the fluid and porous phase in the present study is not significant and so the assumption is valid. The radiation from the permeable cylinder is negligible.

2.2. Conservation equations

Considering above assumptions, the following governing equations are used to represent flow and heat transfer phenomena [51]. Continuity equation:

$$\frac{\partial u^*}{\partial x^*} + \frac{\partial v^*}{\partial y^*} = 0. \tag{1}$$

Momentum equations:

$$\rho\left(\frac{1}{\phi}\frac{\partial u^*}{\partial t} + \frac{u^*}{\phi^2}\frac{\partial u^*}{\partial x^*} + \frac{v^*}{\phi^2}\frac{\partial u^*}{\partial y^*}\right) = -\frac{\partial p^*}{\partial x^*} + \frac{\mu_e}{\phi}\left(\frac{\partial^2 u^*}{\partial x^{*2}} + \frac{\partial^2 u^*}{\partial y^{*2}}\right)$$
$$- \frac{\mu}{K}u^* - \frac{\rho F_s}{\sqrt{K}}|\vec{U}|u^*. \tag{2}$$

$$\rho\left(\frac{1}{\phi}\frac{\partial v^*}{\partial t} + \frac{u^*}{\phi^2}\frac{\partial v^*}{\partial x^*} + \frac{v^*}{\phi^2}\frac{\partial v^*}{\partial y^*}\right) = -\frac{\partial p^*}{\partial y^*} + \frac{\mu_e}{\phi}\left(\frac{\partial^2 v^*}{\partial x^{*2}} + \frac{\partial^2 v^*}{\partial y^{*2}}\right) - \frac{\mu}{K}v^*$$
$$- \frac{\rho F_s}{\sqrt{K}}|\vec{U}|v^* + \rho g\beta(T - T_\infty). \tag{3}$$

where μ_e is the effective dynamic viscosity, p^* is the dimensional pressure and $F_s = \frac{1.75}{\sqrt{150}}\frac{1}{\phi^{3/2}}$ is the inertial factor defined by Fu et al. [52].

Energy equation:

$$\rho C_p \frac{\partial T}{\partial t} + \frac{\rho C_p}{\phi}\left(u^*\frac{\partial T}{\partial x^*} + v^*\frac{\partial T}{\partial y^*}\right) = k_e\left(\frac{\partial^2 T}{\partial x^{*2}} + \frac{\partial^2 T}{\partial y^{*2}}\right). \tag{4}$$

The above governing equations can be written in the non-dimensional form by introducing the following characteristic scales:

$$x = \frac{x^*}{H}, \quad y = \frac{y^*}{H}, \quad \tau_t = \frac{t_\infty}{H}, \quad p = \frac{p^*}{\rho v_\infty^2}, \quad u = \frac{u^*}{v_\infty},$$
$$v = \frac{v^*}{v_\infty}, \quad \theta = \frac{T - T_\infty}{T_W - T_\infty}.$$

Thus, the non-dimensional governing equations of macroscopic scale can be written as follows:

$$\frac{\partial u}{\partial x} + \frac{\partial v}{\partial y} = 0. \tag{5}$$

$$\frac{\partial u}{\partial \tau_t} + \frac{1}{\phi}\left(u\frac{\partial u}{\partial x} + v\frac{\partial u}{\partial y}\right) = -\phi\frac{\partial p}{\partial x} + \frac{\Lambda}{Re}\left(\frac{\partial^2 u}{\partial x^2} + \frac{\partial^2 u}{\partial y^2}\right)$$
$$- C_1\phi\frac{1}{ReDa}u - C_2\frac{1.75}{\sqrt{150}}\frac{1}{\sqrt{Da}}$$
$$\times \frac{\sqrt{u^2 + v^2}}{\sqrt{\phi}}u. \tag{6}$$

$$\frac{\partial v}{\partial \tau_t} + \frac{1}{\phi}\left(u\frac{\partial v}{\partial x} + v\frac{\partial v}{\partial y}\right) = -\phi\frac{\partial p}{\partial y} + \frac{\Lambda}{Re}\left(\frac{\partial^2 v}{\partial x^2} + \frac{\partial^2 v}{\partial y^2}\right)$$
$$- C_1\phi\frac{1}{ReDa}v - C_2\frac{1.75}{\sqrt{150}}\frac{1}{\sqrt{Da}}$$
$$\times \frac{\sqrt{u^2 + v^2}}{\sqrt{\phi}}v + \phi Ri\theta. \tag{7}$$

$$\frac{\partial \theta}{\partial \tau_t} + \frac{1}{\phi}\left(u\frac{\partial \theta}{\partial x} + v\frac{\partial \theta}{\partial y}\right) = \frac{R_k}{Re \cdot Pr}\left(\frac{\partial^2 \theta}{\partial x^2} + \frac{\partial^2 \theta}{\partial y^2}\right). \tag{8}$$

Here, C_1 and C_2 are the binary constants which hold the value of 0 at clear fluid zone and 1 at the porous zone. The dimensionless variables are defined as: $Pr = \mu C_p/k$ is the Prandtl number, $\Lambda = \mu_e/\mu$, denotes the viscosity ratio, $Ri = Gr/Re^2$ is the Richardson number. The viscosity ratio and thermal conductivity ratio are assumed to be unity in the present study.

2.3. Lattice Boltzmann Method [LBM]

LBM is a kinetic based mesoscopic approach that can be viewed as a special discrete scheme for the Boltzmann equation with discrete velocities. In LBM, a single particle distribution function is used to model the fluid. It exhibits many advantages over the conventional computational fluid dynamics. In LB equation the convective term (i.e. streaming equation) is linear. Whereas, it is nonlinear in case of Navier stokes equations. Complex boundary conditions can be easily implemented by using particle reflection rule. The conventional numerical methods usually needs more computations to solve the Poisson equation for the pressure field of the incompressible flows while in LB method the fluid pressure can be easily formulated with an equation of state [32].

2.3.1. LB equation for velocity field

In the traditional lattice Boltzmann method, the particles at each node undergo collision followed by streaming. The extended LB collision equation for the porous medium [43] can be expressed as

$$f_i(x + e_i\Delta t, t + \Delta t) - f_i(x,t) = -\frac{1}{\tau}[f_i(x,t) - f_i^{eq}(x,t)] + \Delta t F_i$$
$$+ \Delta t F_b. \tag{9}$$

In Eq. (9), f_i is the instantaneous particle density at a link, f_i^{eq} is the corresponding equilibrium density and e_i are the velocity direction vectors of the particles residing in the lattice. In this study, D2Q9 lattice arrangement which has eight particles around the central particle has been used. The speeds of the particles can be written as

$$e_i = \begin{cases} (0,0), & i = 0 \\ (cos[(i-1)\pi/2], sin[(i-1)\pi/2])e, & i = 1-4 \\ (cos[(2i-9)\pi/4], sin[(2i-9)\pi/4])\sqrt{2e}, & i = 5-8. \end{cases} \tag{10}$$

Also, the right side term of this collision equation is the BGK collision operator or Single Relaxation Time (SRT). In SRT model, the population of particles resides in a single lattice are relaxed towards equilibrium with the same relaxation time. The relaxation factor 'τ' relaxes the particles towards to the equilibrium value during the collision of particles. The Chapman-Enskog relation relates the LB fluid viscosity and the non-dimensional relaxation time and it can be written as

$$v = \left(\tau - \frac{1}{2}\right)\Delta t c_s^2 \tag{11}$$

A force term F_i which accounts the drag effects due to the presence of porous medium is directly coupled with the BGK collision

operator to recover fluid flow through the porous region. The force term that includes the effect of porosity (ϕ) of the porous medium [43,45] can be written as

$$F_i = w_i \rho \left(1 - \frac{1}{2\tau}\right) \left[3(e_i.F) + \frac{9}{\phi}(e_i.U)(e_i.F) - \frac{3}{\phi}(U.F)\right]. \tag{12}$$

Here, F is the body force due to the presence of porous medium which is otherwise termed as Darcy-Forchheimer force term [43]. This can be written as

$$F = -\frac{\phi v}{K} U - \frac{\phi c_F}{\sqrt{K}} |U|U + \phi G. \tag{13}$$

where v is the kinematic viscosity of the fluid, K is the permeability of the porous medium, c_F is the non-dimensional Forchheimer form-drag coefficient or inertial factor, $|U| = \sqrt{u^2 + v^2}$ in which u and v are the components of U in the x- and y-directions, and G is the body force due to gravity. The equilibrium distribution function which appears on the right side of Eq. (9) should consider the porosity of the porous medium. It can be written as follows:

$$f_i^{eq} = w_i \rho \left[1 + 3(e_i \cdot U) + \frac{9}{2\phi}(e_i \cdot U)^2 - \frac{3}{2\phi}(U \cdot U)\right]. \tag{14}$$

The weighing factors w_i are an important part in the calculation of equilibrium distribution functions. Each particle residing in the lattice will have its own weighing factor. In case of D2Q9, $w_0 = 4/9$, $w_i = 1/9$ for i = 1–4 and $w_i = 1/36$ for i = 5–8. After performing the simulation in the mesoscopic level, the macroscopic properties needs to be calculated. The addition of distribution function of each lattice represents density of the fluid. This relationship between the distribution function and density is very helpful in finding out the macroscopic properties such as density and velocity of the fluid. Density ρ and velocity u can be evaluated from the distribution function as follows:

$$\rho = \sum_{i=0}^{8} f_i. \tag{15}$$

The auxiliary velocity V can be defined as

$$\rho V = \sum_{i=1}^{8} e_i f_i + \frac{\Delta t}{2} \rho F. \tag{16}$$

The actual velocity components of porous medium can be calculated from the following equation:

$$U = \frac{V}{c_0 + \sqrt{c_0^2 + c_1 |V|}}. \tag{17}$$

The two parameters c_0 and c_1 in Eq. (17) are given by

$$c_0 = \frac{1}{2}\left(1 + \phi \frac{\Delta t}{2} \frac{v}{K}\right); c_1 = \phi \frac{\Delta t}{2} \frac{c_F}{\sqrt{K}}. \tag{18}$$

To analyse forced convection, a separate distribution function is used and to show the effects of natural convection, an extra force term (F_b) is added to the LB collision equation, because the flow in this case is driven by temperature gradient. The Boussinesq approximation in LB can be written as follows:

$$F_b = 3w_i g \beta \theta e_{iy}. \tag{19}$$

Here, e_{iy} is the velocity vectors acting in the y-direction.

2.3.2. LB equation for temperature field

To evaluate the temperature physiognomies, one more distribution function called $g(x,t)$ is used. In both forced and mixed convection, the energy equation can be solved after flow field is calculated. The macroscopic values obtained from the flow field

distribution functions $f(x,t)$ are then used in the temperature distribution function $g(x,t)$. The LB equation that describes the temperature filed can be written as

$$g_i(x + e_i \Delta t, t + \Delta t) - g_i(x,t) = -\frac{1}{\tau'}[g_i(x,t) - g_i^{eq}(x,t)]. \tag{20}$$

Here, τ' is the dimensionless relaxation time and it is evaluated from thermal diffusion coefficient ($\alpha = v/Pr$). The Chapman-Enskog relationship for thermal relaxation time can be written as

$$\alpha = \left(\tau' - \frac{1}{2}\right)\Delta t c_s^2. \tag{21}$$

The temperature equilibrium distribution function g_i^{eq} in the Eq. (20) can be written as

$$g_i^{eq} = w_i T[1 + 3(e_i.U)]. \tag{22}$$

In the above equation, w_i is the same weighing factors which has been defined in the flow equilibrium distribution function and T is the temperature of the fluid. The temperature T can be calculated from the distribution function $g(x,t)$ as

$$T = \sum_{i=0}^{8} g_i. \tag{23}$$

2.3.3. Boundary conditions

In practical cases, the boundary conditions are applied in terms of macroscopic variables like ρ and U. This Lattice Boltzmann simulation has the information of particle distribution functions before calculating the macroscopic values. Therefore, boundary conditions also need to be specified in terms of distribution functions only. Various boundary conditions used in this study are described below.

Inlet boundary condition: The flow simulated by LB method is weekly compressible and hence, the inlet velocity has to be chosen as Mach number (Ma), less than 0.1 [32]. A free uniform velocity (v_∞), which has less compressibility effects is given to the inlet and it can be indicated as v_0. The distribution functions f_2, f_5 and f_6 fall inside the domain at the inlet region (bottom of the computational domain). The Zou and He boundary condition [53] is applied to inlet of the domain to find out the unknown distribution functions and it can be written as follows:

$$\rho_0 = \frac{1}{1 - v_0}[f_0 + f_1 + f_3 + 2(f_4 + f_7 + f_8)]. \tag{24}$$

$$f_2 = f_4 + \frac{2}{3}\rho_0 v_0; \quad f_5 = f_7 + \frac{1}{6}\rho_0 v_0; \quad f_6 = f_8 + \frac{1}{6}\rho_0 v_0. \tag{25}$$

In the above equation ρ_0 and v_0 are the initial density and velocity (in y-direction) respectively.

Left and Right boundary: The study aims to simulate flow around and through the square porous cylinder in the unconfined domain. Artificial left and right boundaries are placed far away from the cylinder in order to avoid the shear stress developed by the walls. Accordingly, the slip boundary condition needs to be adopted to satisfy this requirement. In case of left boundary, the unknown distribution functions are f_1, f_5 and f_8. As per the slip condition [54], for the entire length of left boundary the following conditions are used. $f_{(1,x)} = f_{(1,x-1)}$, $f_{(5,x)} = f_{(5,x-1)}$ and $f_{(8,x)} = f_{(8,x-1)}$.

Outlet boundary condition: General practice of evaluating the unknown distribution functions at the outlet is through extrapolation [32]. At the outlet of the domain the unknown distributions are f_4, f_7 and f_8 which can be evaluated by using second order polynomial.

The porous square region is kept at the non-dimensional temperature value of 1 (i.e. θ = 1).

2.4. Dimensionless parameters

Some of the dimensionless parameters used in this study are defined as follows:

The dimensionless parameters Reynolds number (Re) and Darcy number (Da) are written in terms of lattice numbers.

$$Re = \frac{v_\infty H}{v} = \frac{v_\infty N}{v}. \tag{26}$$

where the height of the cylinder 'H' is the characteristic length and the free stream velocity 'v_∞' is the characteristic velocity. The porosity (ϕ) and Darcy number (Da) could be related through the Carman-Kozeny relation [4] given by,

$$Da = \frac{1}{180} \frac{\phi^3 d_p^2}{H^2(1-\phi)^2} = \frac{K}{H^2} = \frac{K}{N^2}. \tag{27}$$

In LBM, the numerical stability and accuracy of the results are mainly dependent on the number of lattices on characteristic length and in present analysis; N represents the number of lattices that are present on the front face of the cylinder. In this study we have taken the particle diameter (d_p) as 1 cm (for H = 1 m) [55].

The dimensionless stream function ψ is defined as

$$u = \frac{\partial \psi}{\partial y} \quad \text{and} \quad v = -\frac{\partial \psi}{\partial x}. \tag{28}$$

The curl of the flow velocity or vorticity (ω) for two-dimensional flows can be evaluated as

$$\omega = \frac{\partial v}{\partial x} - \frac{\partial u}{\partial y}. \tag{29}$$

Heat transfer from a permeable body to the surrounding fluid is evaluated from the local Nusselt number is given by $Nu = -R_k \frac{\partial \theta}{\partial n}$. Here, n is the direction normal to the body surface and R_k is the ratio of thermal conductivity of the porous material and fluid, which is assumed to be 1 in this study. Average heat transfer at any face of the permeable body is obtained by integrating the local Nusselt number along that face. The surface averaged Nusselt number on the front (f), rear (r), left ($s1$) and right ($s2$) face of the cylinder (see Fig. 2) is calculated as

$$Nu_f = -\int_A^B Nu \cdot dx; \quad Nu_r = -\int_C^D Nu \cdot dx;$$
$$Nu_{s1} = -\int_D^A Nu \cdot dy \quad \text{and} \quad Nu_{s2} = -\int_B^C Nu \cdot dy. \tag{30}$$

The mean Nusselt number value (Nu_M), which represents the total heat transfer from the permeable cylinder is evaluated from the average Nusselt number of all surfaces as shown below

$$Nu_M = \frac{1}{4} \sum_{AB} Nu_{f,r,s1,s2}. \tag{31}$$

The heat transfer enhancement obtained by permeable cylinder with respect to solid cylinder (or permeable cylinder with $Da = 10^{-6}$) is expressed in terms of Heat Transfer Enhancement Ratio (E). It is given by the ratio of Nusselt number of any permeable cylinder to Nusselt number of permeable cylinder with $Da = 10^{-6}$.

$$E = \frac{(Nu)_{\text{at any value of } Da}}{(Nu)_{\text{at } Da=10^{-6}}}. \tag{32}$$

The present study elaborates on the variation of E at different faces of the cylinder and, hence, heat transfer enhancement ratio at different faces is represented as E_f, E_r, E_{s1} & E_{s2} for front, rear, left and right faces, respectively.

3. Numerical procedure and validation

3.1. Numerical method

A FORTRAN code has been written based on lattice Boltzmann method to perform the present numerical simulations. The collision equation with the external force term (F_i) (Eq. (9)) is applied to the entire computational domain. A constant value of 1 is multiplied with this force term in the porous square region. In all other places the porous force term (F_i) is nullified to get the clear fluid region flow. However, the buoyancy force term (F_b) is applied in the entire domain. In this study, BGK collision operator with single non-dimensional relaxation factor (τ) has been used. The initialization process carries the formulation of initial velocity (v_0) and LB kinematic viscosity based on the number of lattices on characteristic length (N). Through Chapman-Enskog relationship [56] the relaxation factors ($\tau \& \tau'$) are calculated. Initially, the velocities (i.e. u and v) at all nodes are assumed to be zero and the density value ρ is kept 1. The Boussinesq force term which appears in Eq. (9) has $g\beta$ and this can be calculated from Richardson number. It should be noted that the velocity scale is proportional to $\sqrt{g\beta \triangle TH}$. In order to ensure the problem in incompressible regime, the value of $\sqrt{g\beta \triangle TH}$ should be less than 0.1 [32]. It is seen that the numerical algorithm of lattice Boltzmann is relatively simpler than the conventional CFD methods. In the present work, the LBM computations are carried out until the following convergence is satisfied.

$$\frac{\sqrt{\sum_{i,j}\left[U_{i,j}^{k+1} - U_{i,j}^k\right]^2}}{\sqrt{\sum_{i,j}\left[U_{i,j}^{k+1}\right]^2}} \leqslant 1 \times 10^{-6}, \frac{\sqrt{\sum_{i,j}\left[T_{i,j}^{k+1} - T_{i,j}^k\right]^2}}{\sqrt{\sum_{i,j}\left[T_{i,j}^{k+1}\right]^2}} \leqslant 1 \times 10^{-6}. \tag{33}$$

where $U_{i,j}$ is the fluid velocity, $T_{i,j}$ is the fluid temperature and k is the iteration level.

3.2. Mach number annealing

In lattice Boltzmann, the compressibility errors can be reduced significantly by reducing Mach number (Ma). This unfortunately blows up the computational time needed for convergence [57]. Hence, in case of low Re flows, for the same values of characteristic length (H), the initial velocity (v_0) has to be reduced. It implies that the $Ma(=v/c_s)$ is actually getting reduced. To accelerate the simulations even at low velocities, Artoli et al. [58] have proposed an idea which is based on stepwise reduction of Ma after the simulation converges at higher value of Mach number. In order to perform simulation at low Ma, the velocity v_0 and consequently the viscosity (v) have to be reduced to produce the same Re. Since Ma is reduced in steps, this technique is called Mach number annealing. The annealing factor n can be define as

$$n = \frac{Ma}{Ma'} = \frac{v}{v'} = \frac{v}{v'}. \tag{34}$$

This equation implies that all the velocity (in terms of driving force) and the viscosity values are to be reduced n times. This annealing can be of single (direct) and multilevel. In one level annealing strategy, after the simulation converges with a higher Mach number, the viscosity and driving force are reduced n times in a single step and the simulation converges to the final solution. The gradual reduction of these parameters towards n is followed in case of multilevel annealing. This level of annealing is mainly dependent on the stability and tolerance constraints. In this study, we have used direct or single step annealing to accelerate the simulation. The non-dimensional relaxation values for hydrodynamic (τ) and thermal (τ') are taken as 0.56 and 0.5845, respectively.

3.3. Grid sensitivity analysis

A lattice sensitivity study is carried out at $Re = 40$, $Da = 10^{-6}$ and $Ri = 1$ to check the dependence of flow and heat transfer parameters such as C_D and Nu_M on the number of lattice units and downstream length (L_D). Based on number of lattice units on characteristic length, the relaxation parameter (τ) that appears in the collision equation changes and so the stability and accuracy of the solution. Although more number of lattices could deliver accurate results, the convergence rate of numerical solution slows down due to the decrement of initial velocity value. A systematic test simulations have been performed with 20–40 lattice units on front face of the cylinder and is presented in Table 1. The simulation running time at $L_D = 30$ is noticed to be 37.35, 44.25, 51.45, 60.3, 72.4 and 84.2 h for N = 20, 24, 28, 32, 36 and 40, respectively. Also, the results obtained at this downstream length has shown less variations with $L_D = 40$. Hence, the study suggest that, the grid size of 1312×960 (32 lattices on characteristic length) with downstream length of 30D will produce results independent of lattice units with less computational time.

3.4. Code validation

The numerical results obtained from present LBM code with air as a working fluid ($Pr = 0.71$) is compared with the studies available in the literature at $5 \leqslant Re \leqslant 40$, $Da = 10^{-3}$ and 10^{-2} and $Ri = 0$ and 1. To consider the variation of both permeability and buoyancy conditions, different aforementioned parameters have been chosen to compare with the available literatures. In Fig. 3 (a), the obtained drag coefficient from present code is compared with the results of Dhinakaran and Ponmozhi [51], Sharma and Eswaran [59], Paliwal et al. [60] and Sharma et al. [29]. Fig. 3(b) graphically showing the comparison of mean Nusselt number obtained from the present code with above literatures at different permeability levels and buoyancy condition. The graphical illustration clearly represents that the present numerical results for C_D and Nu_M are in good agreement with the results available in the literature. A maximum error of 1.4% and 3.4% is obtained in the case of drag coefficient and mean Nusselt number, respectively, and this deviation is due to the numerical approach and discretization schemes. It is noteworthy that the literatures considered for numerical result comparison have used finite volume approach; whereas, the present results are simulated from lattice Boltzmann method.

4. Numerical results and discussions

The 2-D numerical simulations are carried out for flow across a permeable square cylinder in an unconfined vertical flow regime, under the influence of aiding buoyancy for the following range of physical parameters:
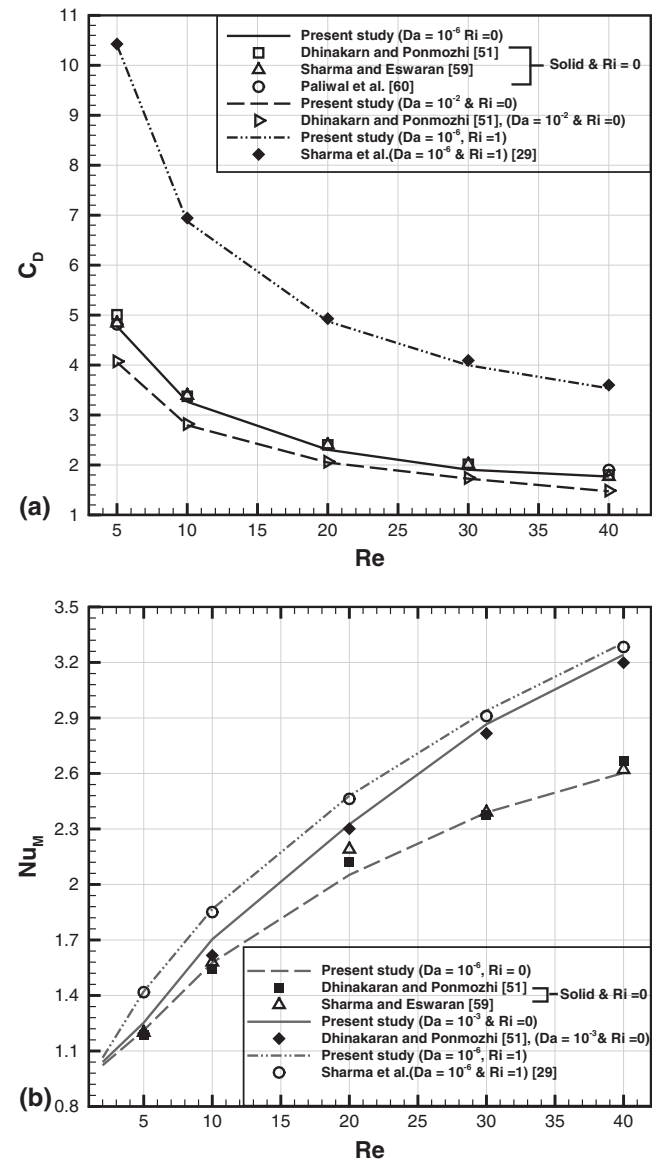

Fig. 3. Comparison of present study results with literature for $Pr = 0.71$: (a) Drag coefficient (C_D) and (b) Mean Nusselt number (Nu_M) at different values of Da and Ri.

- Reynolds number, $Re = 2$–40.
- Richardson number, $Ri = 0$, 0.5 and 1.
- Darcy number, $Da = 10^{-6}$, 10^{-4}, 10^{-3} and 10^{-2}.
- Porosity, $\phi = 0.629$, 0.935, 0.977, 0.993.
- Prandtl number, $Pr = 0.71$(air).

Table 1
Analysis on the effects of number of lattice units (N) and downstream length on drag coefficient (C_D) and mean Nusselt number (Nu_M) at $Re = 40$, $Da = 10^{-6}$, $Pr = 0.71$ and $Ri = 1$.

N	Grid (m × n)	Drag coefficient (C_D)			Mean Nusselt number (Nu_M)		
		$L_D = 20$	$L_D = 30$	$L_D = 40$	$L_D = 20$	$L_D = 30$	$L_D = 40$
20	820 × 600	4.175	4.054	4.055	3.205	3.241	3.241
24	989 × 720	3.612	3.587	3.520	3.225	3.289	3.289
28	1148 × 840	3.701	3.562	3.562	3.255	3.302	3.302
32[a]	1312 × 960	3.570	3.534	3.534	3.266	3.305	3.306
36	1476 × 1080	3.570	3.534	3.534	3.266	3.305	3.306
40	1640 × 1200	3.570	3.534	3.534	3.266	3.305	3.306

[a] Number of lattice units placed on front face of the cylinder in this study.
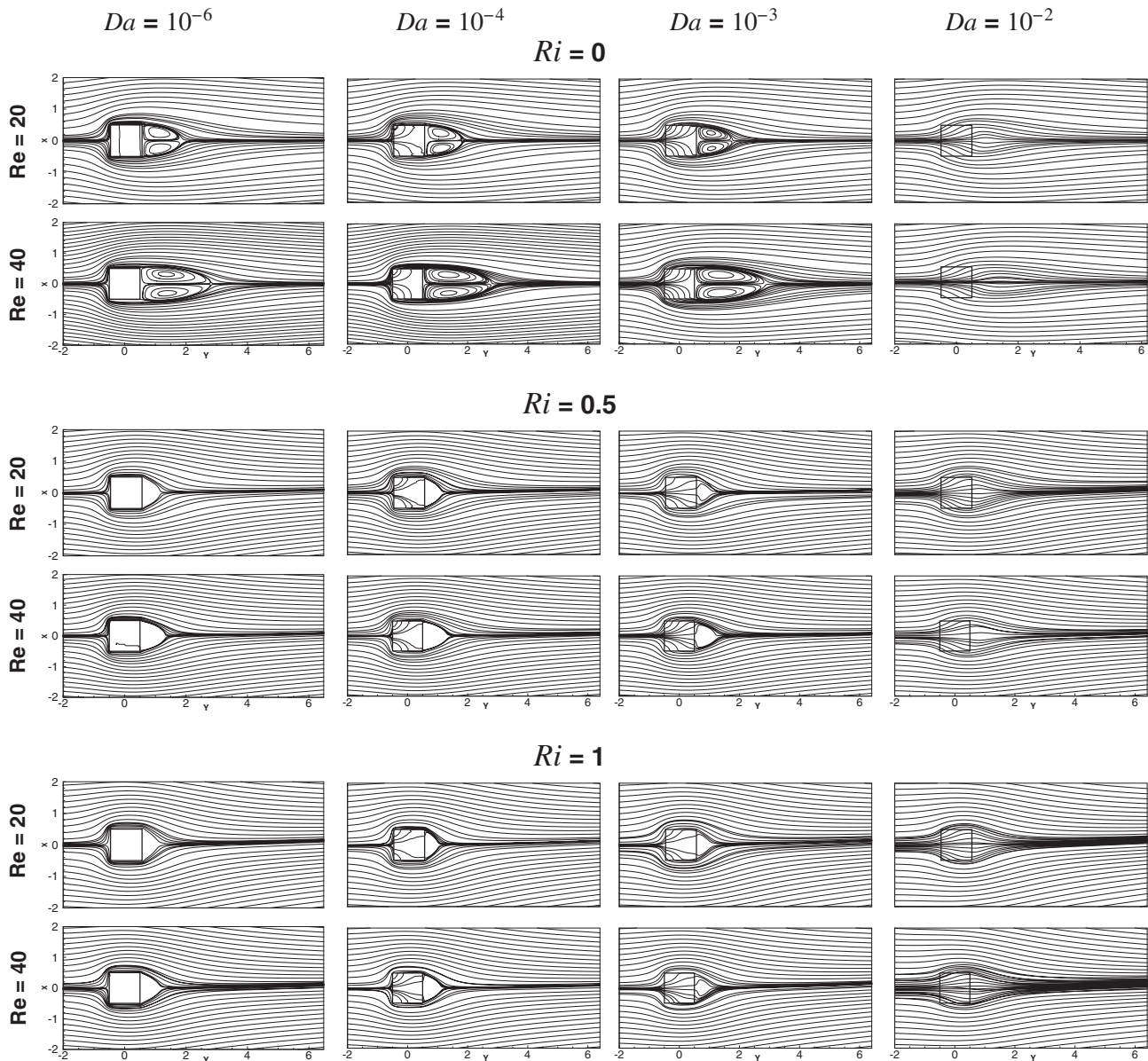
Fig. 4. Streamlines at $Re = 20$ and 40; $Ri = 0$, 0.5 and 1 at various values of Darcy number for the flow around and through the porous square cylinder.

This numerical study will serve us to gauge the effects of buoyancy and permeability on flow and thermal patterns. The results are labelled into flow and heat transfer characteristics and are presented as follows:

4.1. Flow characteristics

A detailed discussion on variation of flow behaviour with Reynolds number (Re), Darcy number (Da) and Richardson number (Ri) is presented in this section.

4.1.1. Streamline pattern

In Fig. 4 we present the representative flow patterns in the vicinity of permeable square cylinder through streamline contours at different values of Reynolds number ($Re = 20$ and 40), Richardson number ($Ri = 0$, 0.5 and 1) and Darcy number ($Da = 10^{-6}$, 10^{-4}, 10^{-3} and 10^{-2}). It is clear that, streamlines are a function of Reynolds number and are also altered with the introduction of different permeability and buoyancy levels. It is seen that at very low Re ($\leqslant 2$), the flow is completely attached to the cylinder due to excess viscous forces on its surface. Upon increasing fluid velocity, the inertial forces become dominant and hence, flow separation takes places at the trailing edge of the cylinder. This phenomenon is common in the case of flow over a solid square obstacle and the same pattern can be observed at $Da = 10^{-6}$ with no buoyancy factor (i.e. $Ri = 0$). Furthermore, the wake length decreases with an increase of Ri for all values of Da (except $Da = 10^{-2}$) at constant Re. At higher buoyancy force, the velocity gradient is more and it results in reduction of pressure over the cylinder. Owing to this, reduction of wake zone is noticed with an increase in Ri. The increment of permeability level gradually allows fluid into the cylinder with different deviation levels. For example, the deviation of flow through the cylinder at $Da = 10^{-4}$ is greater due to the excess viscous drag term when compared with $Da = 10^{-3}$. A closer view of streamline pattern through the permeable cylinder is presented in Fig. 5, which shows the variation of fluid deviation inside the porous zone with permeability and buoyancy. The flow deviation level inside the cylinder also varies due to
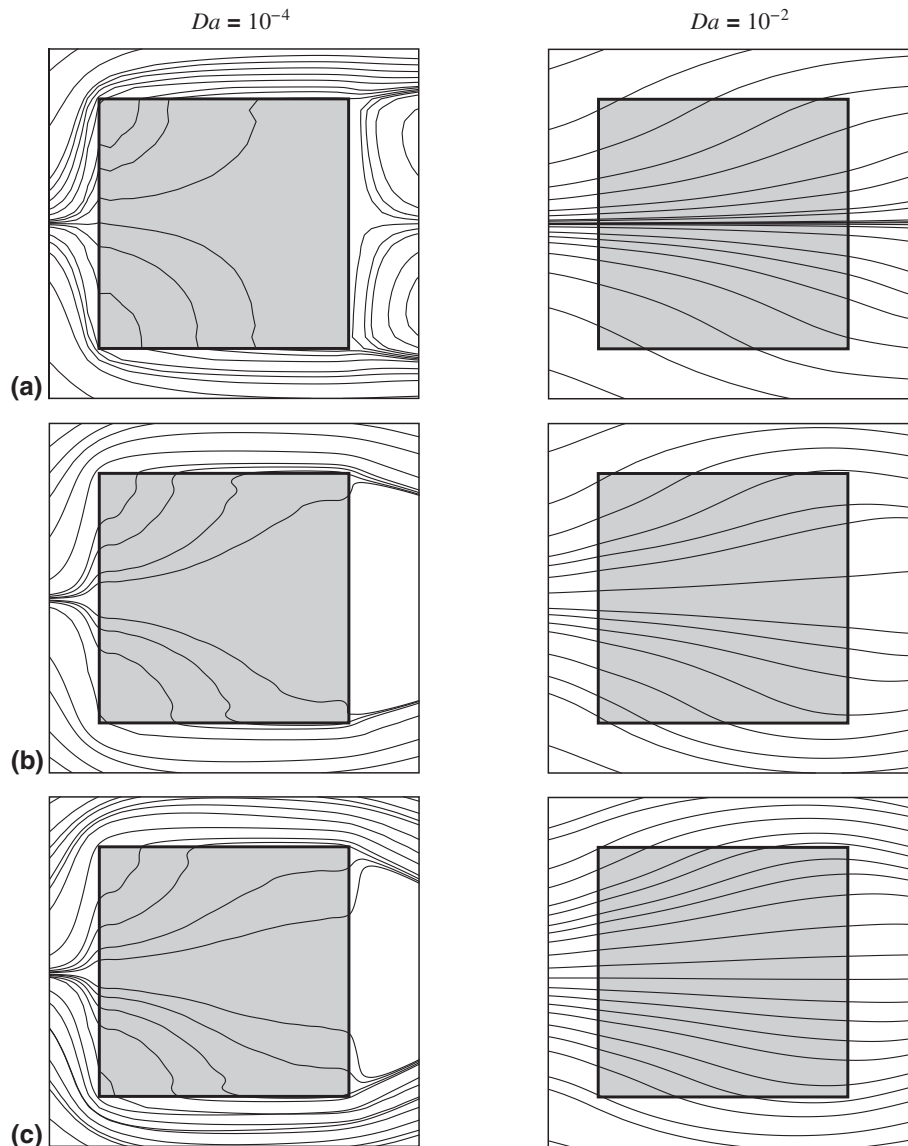
$Da = 10^{-4}$ $\qquad\qquad\qquad\qquad\qquad$ $Da = 10^{-2}$

Fig. 5. A closer view of streamline pattern through the permeable cylinder at Re = 40 for two different Da values and (a) Ri = 0, (b) Ri = 0.5 and (c) Ri = 1.

buoyancy effects. For a fixed Re and Da, upon increasing Ri the flow deviation starts reducing and this is due to the dominance of buoyancy over viscous drag term of porous region. To emphasis this, we present the average normal velocity (U_{avg}) variation over leeward, middle and right/left surface of the cylinder in Fig. 6. The variation of average normal velocity over different surfaces clearly exhibits the influence of permeability and buoyancy. For a constant value of Da and Ri, U_{avg} is higher at the left/right surface followed by middle and leeward surface of the cylinder. This clearly indicates that, due to resistance created by the porous medium, the fluid tends to deviate; consequently, average normal velocity is higher at these surfaces. The velocity of fluid on different surfaces increases with an increase in permeability level and this increment is drastic when the permeability level is shifted from 10^{-3} to 10^{-2}. Hence, more streamlines pass through the cylinder at this level of Da. It can also be seen from Fig. 6 that the average normal velocity increases with increasing buoyancy levels for same value of Da. It is evident that increasing buoyancy can stretch the fluid inside the porous medium with relatively higher velocity. However, for all Re and buoyancy levels the flow is observed to be more elongated at $Da = 10^{-2}$ and there is no wake formation downstream of the

cylinder. Therefore, this streamline flow pattern concludes that the aiding buoyancy and permeability prove to be influential on drag and inertial forces inside the cylinder.

4.1.2. Vorticity pattern

To further provide an insight on the behaviour of fluid flow, especially near the porous square zone, the vorticity patterns are also presented in Fig. 7. The solid and dotted lines in this contour frames indicate positive and negative values of vorticity. The flow phenomenon for different Re has been well elucidated earlier in Section 4.1.1. In this section, effects of Ri and Da on vorticity strength are discussed, and same is presented in Fig. 7 for Re = 40. The intensity of local rotation increases with Re for a constant value of Ri, due to the increase of inertial forces and it decreases with the increasing Ri for a fixed value of Re. The similar behaviour of vorticity pattern with respect to Re and Ri is observed for a long square bar under the influence of buoyancy by Sharma et al. [29]. Considering the effect of Da, the vorticity strength changes due to the variation of fluid penetration. At $Ri = 0$, the changes in permeability at constant Re shows the similar patterns as derived by Dhinakaran and Ponmozhi [51]. At $Da = 10^{-6}$, the
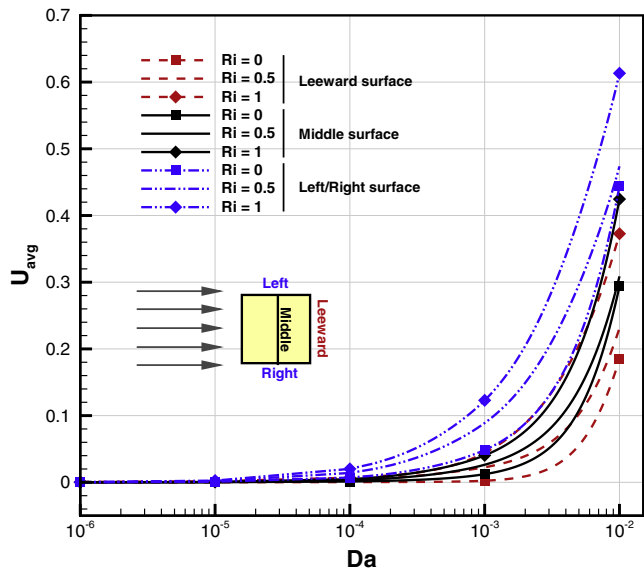
Fig. 6. Average normal velocity (U_{Avg}) along the leeward, middle and right/left surface of the porous square cylinder for different Da and Ri values at $Re = 40$.

4.1.3. Drag coefficient (C_D)

To convey the quantitative effects of Da and Ri at various Re on flow behaviour around and through the permeable cylinder, the coefficient of drag (C_D) variations have been presented in Fig. 8. The drag force experienced by the cylinder is calculated using momentum exchange method [61], in which the exchange of momentum between two opposing directions of the neighbouring lattices are used to evaluate the drag and lift forces. It is a well known fact that, the drag value decreases with the increment in Re due to the depletion of viscous layer around the cylinder. The low fluid resistance inside the porous zone at higher permeability reduces the pressure gradient across the cylinder. This occurrence results in decrement of drag coefficients for all the ranges of buoyancy conditions considered. In short, the drag coefficient decreases with the increase of Da irrespective of Re and/or Ri. At $Re \geqslant 25$, drag values of the cylinder at $Da = 10^{-3}$ approaches lower permeability drag values for all ranges of Ri. At $Da = 10^{-2}$, fluid penetrates with very less deviation inside the cylinder; the cylinder experiences lower drag. The non-linear drag trend, with variation of Re is found to be consistent for all values of Ri. The viscous dominance due to aiding buoyancy increases the drag value of the cylinder for constant Re and Da. Thus, it can be concluded that, the drag coefficient increases with an increase in Ri substantially and the same decreases monotonously while increasing the permeability level.

4.1.4. Recirculation length (L_r)

From the streamline patterns it can be observed that due to dominant inertial forces with the increase in Re, two counter rotating eddies are formed in downstream of the cylinder. The streamwise distance between top surface and wake bubble stagnation point is termed as wake/recirculation length. Fig. 9 neatly presents the variation of wake length with Reynolds number at $Da = 10^{-6}, 10^{-4}$ and 10^{-3} and at $Ri = 0, 0.5$ and 1. The symmetric vortex pair behind the cylinder grows with the increase of Re

vorticity patterns are symmetric along a vertical line and it is completely attached to the cylinder surface. Due to the reduction of viscous resistance and increase in inertial forces, the fluid flow inside the cylinder increases drastically. Therefore, the fluid diffusion inside the cylinder increases with an increase in permeability. It can be concluded from vorticity frames that both buoyancy effects and permeability of the cylinder reduces the strength of vorticity. Buoyancy force degrades the pressure gradient outside the cylinder whereas, more permeable cylinder reduces the viscous drag inside porous zone.
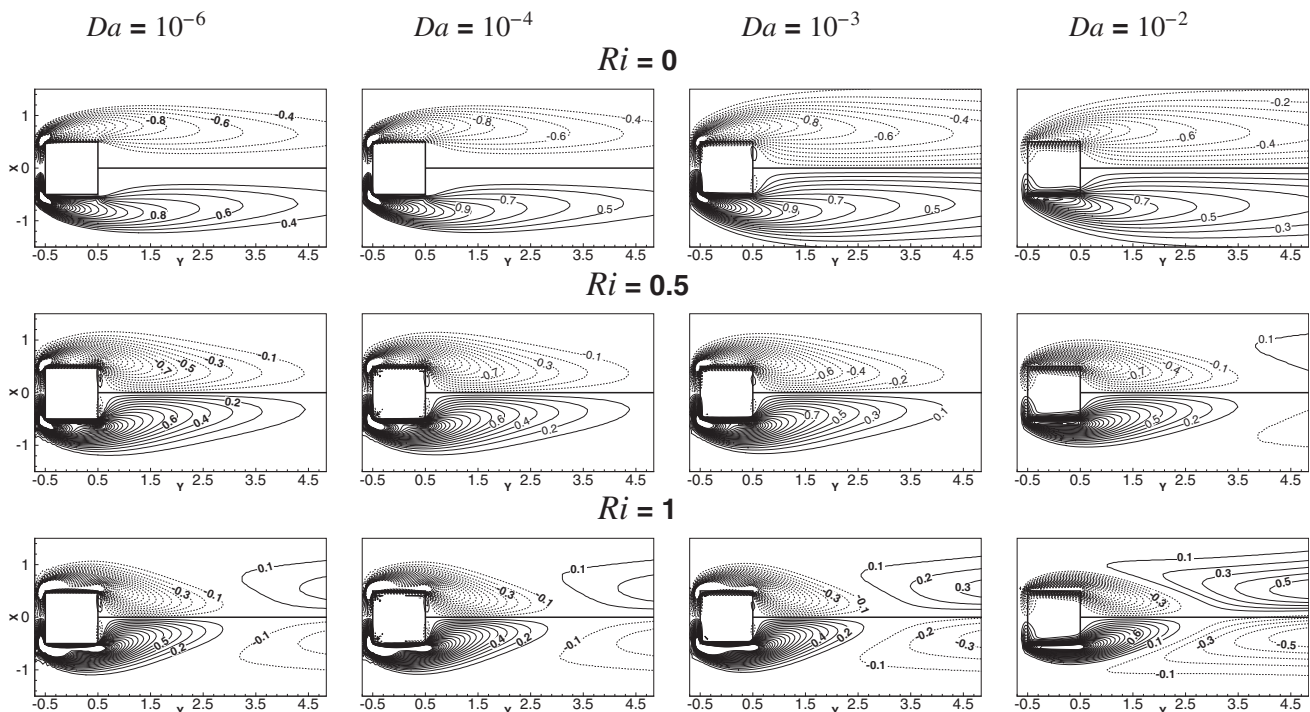

Fig. 7. Vorticity contours at $Ri = 0, 0.5$ and 1; $Re = 40$ at various values of Darcy number for the flow around and through the porous square cylinder.

and it decreases slightly with the introduction of higher permeability. At $Re \geqslant 35$ the stagnation point of wake moves downstream when compared with the lower permeable cylinder (i.e. $Da = 10^{-6}$) for the case of forced convection (i.e. $Ri = 0$). However, the aiding buoyancy cases ($Ri = 0.5$ and 1) have shown inverse trend with the increase in Da for all values of Re. From Fig. 9 it can be understood that buoyancy is more influential on wake length variation than permeability. For fixed values of Re and Da, the wake stagnation point move towards the top surface of the cylinder. The pressure reduction over the cylinder surfaces due to aiding buoyancy is the cause for the streamwise compression of wake bubble. The wake length reduction is found to be largest when the Richardson number increases from 0 to 0.5. The percentage decrement in wake length at $Re = 40$ with $Da = 10^{-3}$ is 494.24%; whereas, the corresponding difference is observed 88.8%. Thus, it can be concluded that buoyancy effect is prominent on wake length reduction than the permeability levels of the porous zone.

4.2. Heat transfer characteristics

Heat transfer characteristics are a function of Reynolds number (Re), non-dimensional permeability (Da) and type of buoyancy condition on the porous cylinder surface. A detailed study on variation of heat transfer performance with aforementioned parameters is presented in this section.

4.2.1. Isotherms

The effect of physical parameters such as Re, Da and Ri on temperature distributions near the porous square zone for the buoyancy aided flow is presented in Fig. 10 for a Prandtl number value of 0.71. The thermal pattern around the cylinder is greatly affected by the Reynolds number, Darcy number and Richardson number. As Re increases, the isotherm pattern spread along the streamwise direction with a subsequent reduction of the lateral width. This is because at higher Re, the convective transport becomes dominant and thermal boundary layer thickness reduces. It can also be seen from Fig. 10 that the size of the thermal plume increases with an increase in Da for a fixed value of Re and Ri. For example, at $Re = 40$, looking at different values of Da in Fig. 10, one can observe the largest thermal plume at $Da = 10^{-2}$ for all values of Ri. As the higher permeable cylinder allows more fluids into it, more heat is dissipated from the cylinder and hence, thermal field is stretched at higher permeability than lower permeability case. Similar patterns have also been reported by Dhinakaran and Ponmozhi [51]. Coming to the effect of buoyancy, the isotherms are more clustered near the surfaces of porous square cylinder with the increase in Richardson number from 0 to 0.5. Also, the thermal plume stretch is large and contract for a constant Reynolds number and Darcy number due to this increment. Therefore, the combined effect of Da and aiding buoyancy has the largest and narrow thermal field which implies higher heat transfer rate. Thus, the reduction of thermal boundary layer around the porous zone due to the higher velocity gradients around the cylinder and dominant inertial forces inside the porous zone results in rich heat transfer performance.

4.2.2. Temperature profile

The influence of Darcy number and aiding buoyancy forces on non-dimensional temperature (θ) profile along the x-direction at $y = 11.5H$ for $Re = 40$ is shown in Fig. 11(a) and (b). In the vicinity of the hot porous cylinder, the non-dimensional temperature value increases and it reaches its maximum value near the centre point, followed by a minor dip at the centre for lower values of Da and at $Ri = 0$. This dip in the middle of domain indicates the reduction of

thermal boundary layer in the region due to fluid recirculation. The value of θ for $Da = 10^{-6}$ along x-axis is almost same as that of $Da = 10^{-4}$. The temperature profile expands further with the increment in Da and it becomes bell-like curve at $Da = 10^{-2}$. This suggests the presence of a thick thermal boundary layer at leeward surface of the cylinder. From Fig. 11(b), one can see the variation of temperature profile with buoyancy. The lateral width of the curve shrinks with the increment in Richardson number. Hence, it is clear that the thermal boundary layer around the cylinder reduces while increasing Richardson number. At higher Ri, more fluid sticks over the cylinder which results in rich heat transfer rate. It is to be noted that the shrinkage of temperature profile is prominent while Ri shifts from 0 to 0.5 and it is less sensitive while it varies from 0.5 to 1.
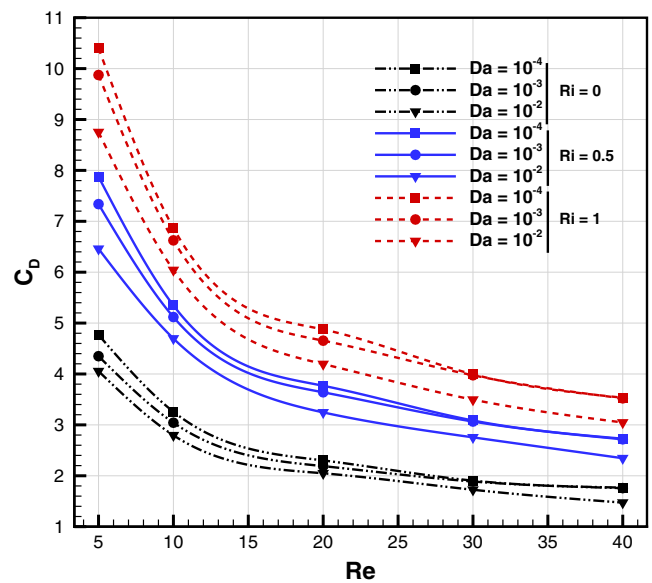
Fig. 8. Variation of drag coefficient (C_D) with Re for different values of Ri and Da, for the flow through and around a porous square cylinder.
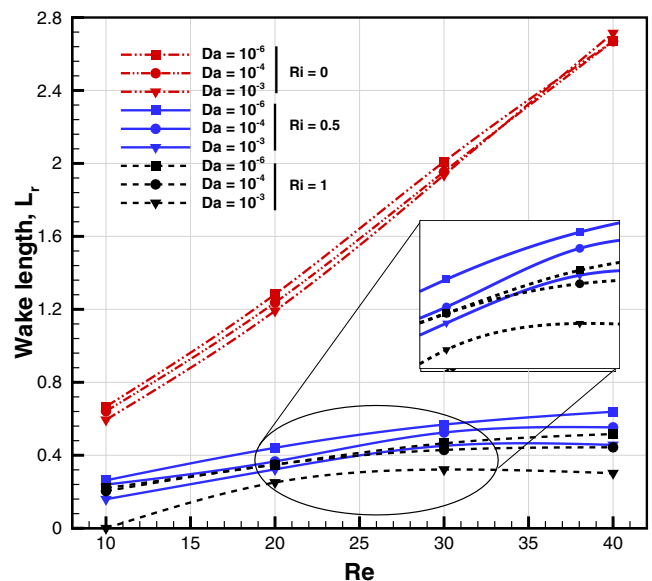
Fig. 9. Wake length (L_r) variation at different values of Re, Da (10^{-6} - 10^{-3}) and Ri (0, 0.5 and 1) for flow around and through porous square cylinder.
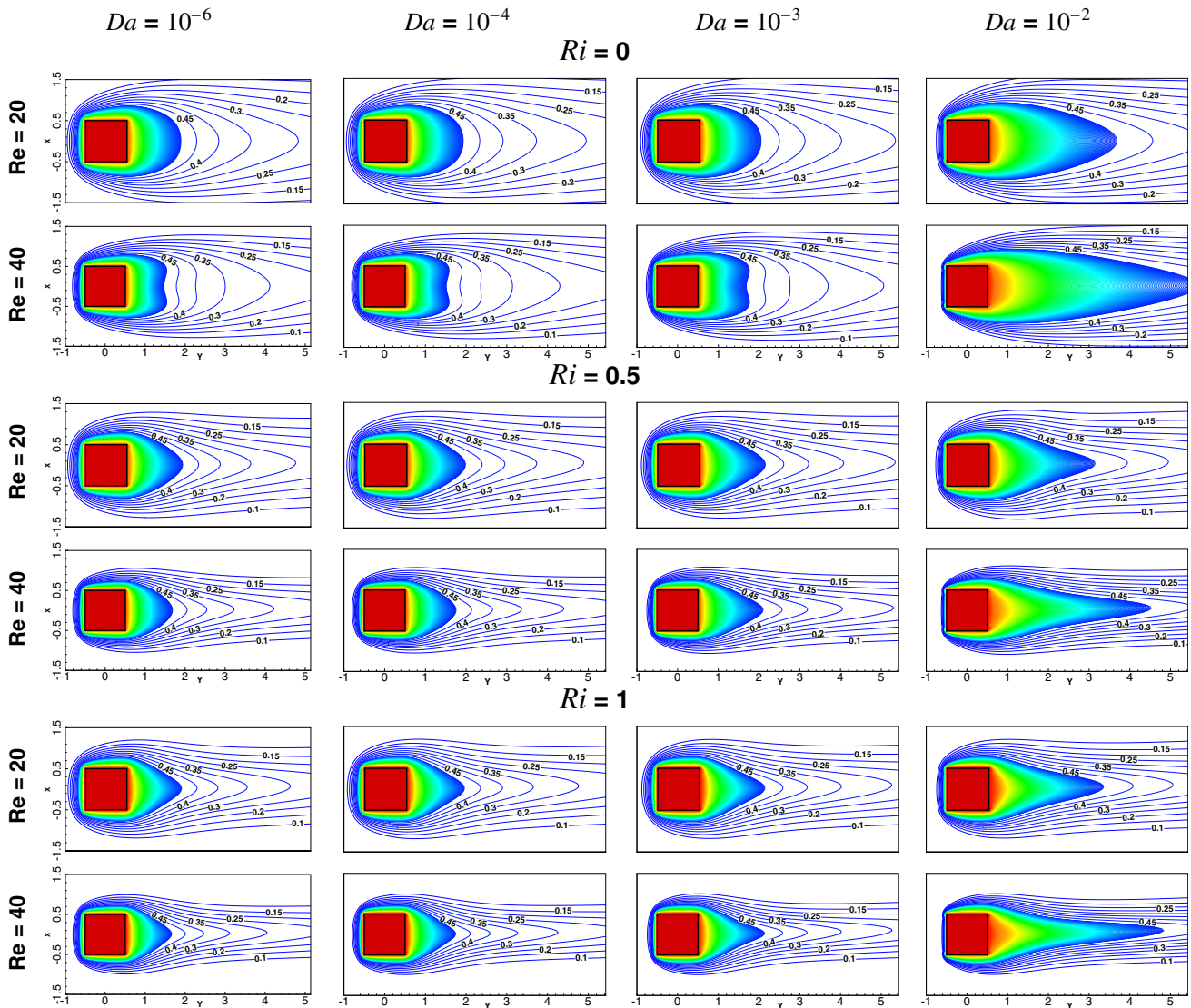
Fig. 10. Isotherms at $Re = 20$ and 40; $Ri = 0,\ 0.5$ and 1 at various Darcy numbers for the flow around and through the porous square cylinder (shaded contour levels between $1 \leqslant \theta \leqslant 0.5$).

4.2.3. Heat transfer enhancement for different faces

Fig. 12(a–c) depict the representative variation of the heat transfer enhancement ratio on each surface of the porous square cylinder for different values of $Re,\ Ri$ and Da. Since it is well known that the heat transfer performance increases with Re, we have presented the effects of aiding buoyancy and Da in terms of heat transfer enhancement ratio (E). The front face of the square cylinder is in direct contact with fluid, and so produces thermal enrichment at this surface compared to other surfaces. It can be observed from Fig. 12(a–c) that at $Da = 10^{-4}$, the heat transfer enhancement ratio is slightly more than 1 for all faces of the cylinder which implies that, at this permeability level the heat transfer augmentation is not much significant. The chance given by front surface to enter more fluid at higher permeability results in rich heat transfer at this surface. Upon increasing Da, the front surface heat transfer enhancement ratio (E_f) increases and it is more drastic when the non-dimensional permeability switches from 10^{-3} to 10^{-2}. The inverse effect on heat transfer enhancement can be observed at rear, left and right surfaces of the cylinder with the increase in Da. At higher permeability levels, from the front surface of the cylinder, more fluid penetrates and carries heat away from it; this

causes heat transfer reduction at all surfaces except front face of the cylinder. The heat transfer enhancement ratio at left/right surface (E_{s1} or E_{s2}) increases at lower values of Re with the increase of Da for all values of Ri and later it reduces with the increase of Da. Looking into the effect of aiding buoyancy with permeability on enhancement ratio (E), the top surface is inversely proportional and at other surfaces it is almost directly proportional to the Darcy numbers. However, it is seen that without the permeability effect, the heat transfer performance at all surfaces increase with the increase of Ri irrespective of Re.

4.2.4. Mean Nusselt number (Nu_M)

The effect of non-dimensional permeability on mean Nusselt number at various values of Re and Ri is illustrated in Fig. 13(a–c). Nu_M increases almost linearly with the increase of Re at all values of Ri and Da. Although different surfaces of the cylinder has shown diverse effects on heat transfer performance with the variations of Darcy number, the mean Nusselt number increases with the increase of the Da. At low values of Re ($2 \leqslant Re \leqslant 10$), there is no significant variation in Nu_M for all values of Da; in this range of Re, only less fluid enters into the cylinder even at higher Da
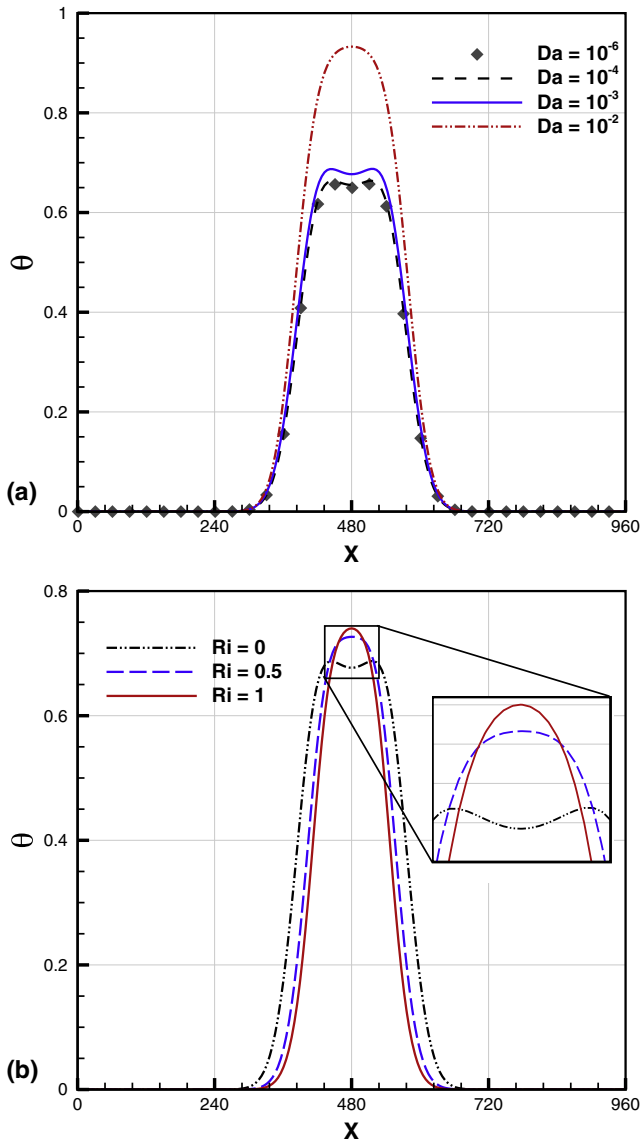
Fig. 11. Influence of (a) Darcy number at $Ri = 0$ and (b) Richardson number at $Da = 10^{-3}$, on the non-dimensional temperature (θ) profile along the direction of x at $y = 11.5H$ for $Re = 40$.

values due to low momentum of the fluid particles. Heat transfer rate is more prominent at higher values of Re for variation of Da and the same has been reported by Dhinakaran and Ponmozhi [51]. One can observe from Fig. 13(a–c) that the Nu_M value of $Da = 10^{-4}$ is close to $Da = 10^{-6}$ at $Ri = 0$ and the gap between these two Da levels increases with the increase in Richardson number. For example, the percentage increase in mean Nusselt number at $Re = 40$, $Da = 10^{-4}$ at $Ri = 0,0.5$ and 1 is 2.04%, 2.2% and 3.03% respectively, compared to solid cylinder. The reduction in thermal boundary layer due to higher velocity gradients at higher Ri is the cause for such heat transfer enhancement. From this section, we can conclude that, the heat transfer performance can be augmented by increasing permeability as well as aiding buoyancy.

The following nonlinear regression correlations are established for the calculation of Nusselt number for the intermediate values of Reynolds number ($2 \leqslant Re \leqslant 40$) and Darcy number ($10^{-6} \leqslant Da \leqslant 10^{-2}$).
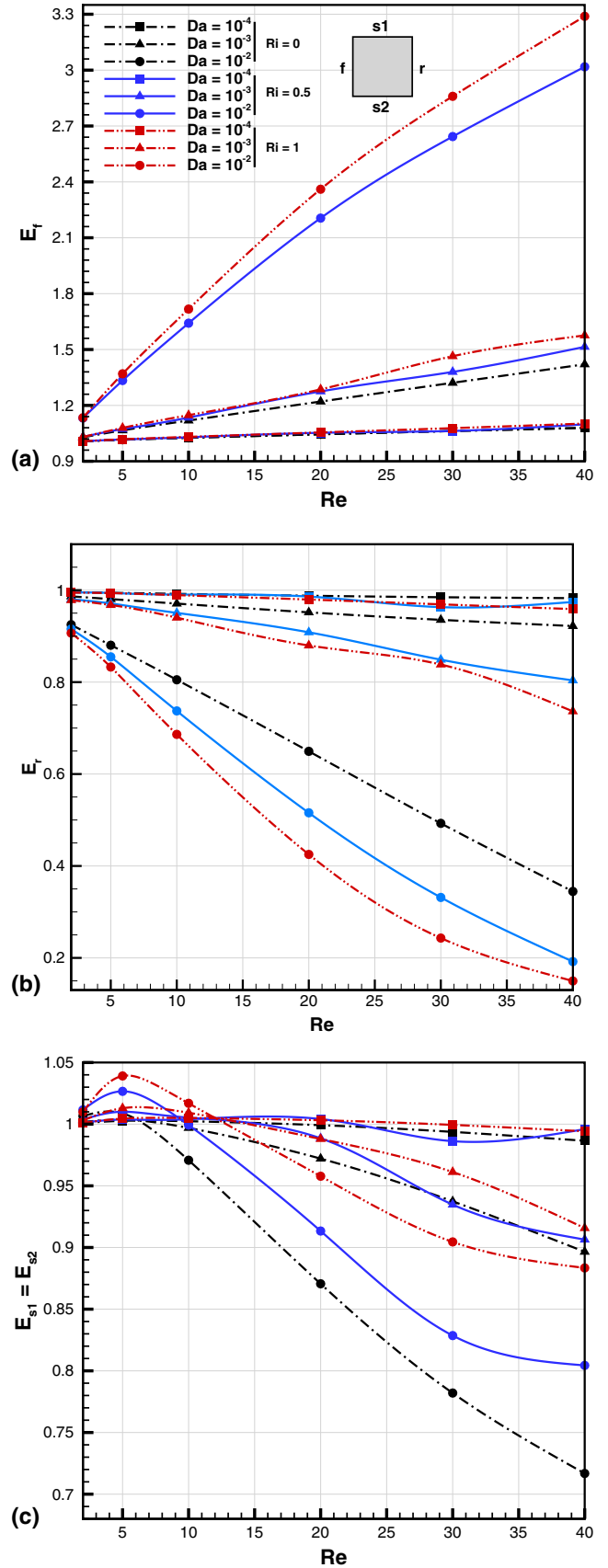

Fig. 12. Effect of Darcy number on heat transfer enhancement ratio at different Reynolds number and Richardson number on (a) front face (b) rear face and (c) left/ right face of the heated porous square cylinder in an unbounded domain.
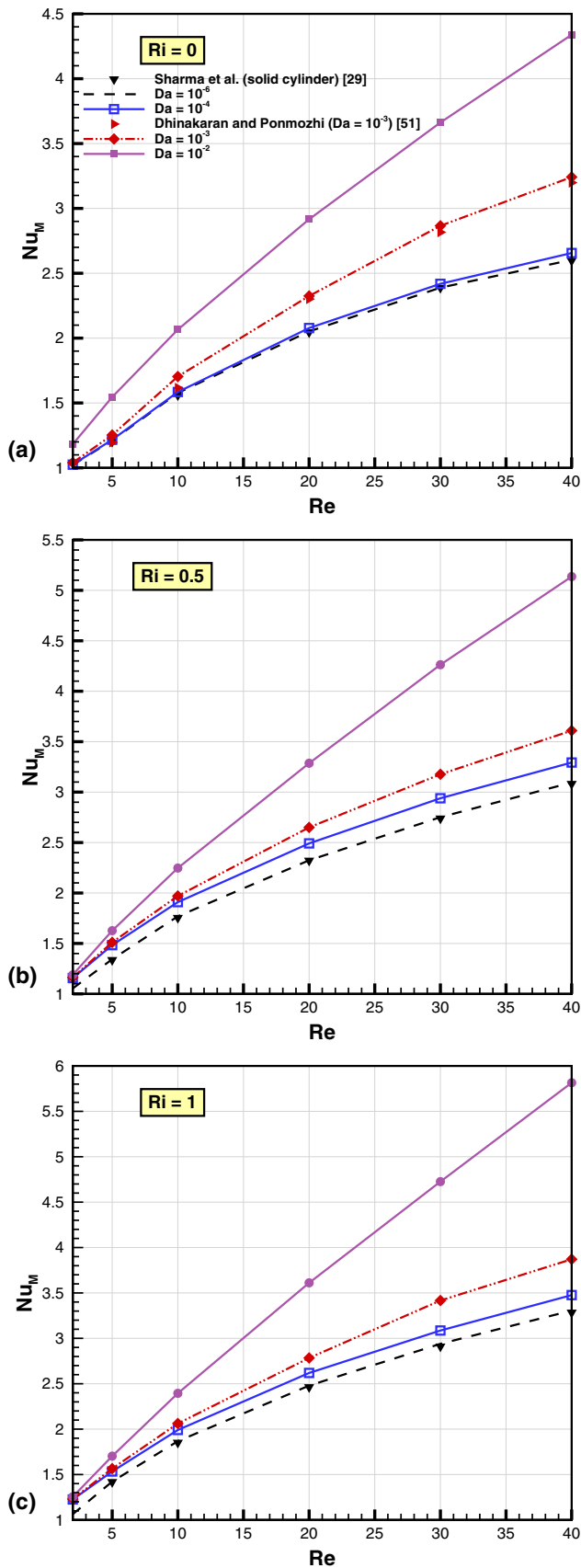
Fig. 13. Effect of Darcy number on mean Nusselt number (Nu_M) at different Reynolds numbers for flow through and around a porous square cylinder in an unbounded domain at (a) $Ri = 0$, (b) $Ri = 0.5$ and (c) $Ri = 1$.

$$Nu_M = 1.258 * Re^{0.696} * \left(\sqrt{Da} + 0.116\right) + 0.761 \quad \text{for} \quad Ri = 0. \tag{35}$$

$$Nu_M = 1.260 * Re^{0.739} * \left(\sqrt{Da} + 0.118\right) + 0.835 \quad \text{for} \quad Ri = 0.5. \tag{36}$$

$$Nu_M = 1.305 * Re^{0.784} * \left(\sqrt{Da} + 0.103\right) + 0.902 \quad \text{for} \quad Ri = 1. \tag{37}$$

The above correlations (Eqs. (35)–(37)) have the correlation coefficient (R^2) values of 0.995, 0.995 and 0.993 with the computed numerical data for the Richardson number of 0, 0.5 and 1, respectively. However, a common expression for different values of Ri with maximum deviation of 8.77% is also been formulated as

$$Nu_M = 1.062 * Re^{0.746} * \left([1 + Ri]^{0.444}\right) * \left(\sqrt{Da} + 0.111\right) + 0.839. \tag{38}$$

5. Conclusion

The flow and heat transfer characteristics of a 2-D porous square cylinder placed in a uniform flow has been analysed in detail under the influence of aiding buoyancy using lattice Boltzmann method. Darcy-Forchheimer terms that corresponds to viscous and inertial effects due to porous medium, is coupled with the SRT collision equation of LBM for porous zone simulation. The outcomes of this numerical investigation can be summarized as follows:

- At lower values of Da ($\leqslant 10^{-6}$), the permeable cylinder behaves like a solid cylinder as the flow restriction is more. Rich permeable cylinder reduces the recirculation zone that forms behind the cylinder and at higher Da ($= 10^{-2}$) no wake forms behind the cylinder. The inertial forces inside the porous cylinder increases as Da increases; which makes the flow less deviated inside the porous zone at higher values of Da. The vortex diffusion is more inside the higher permeable cylinder due to the decrement of resistance to the flow and higher inertial force of the porous zone.
- For the same level of Da and Re, the deviation of fluid is found to be more elongated inside the cylinder at higher values of $Ri > 0$. The higher velocity gradients due to the aiding buoyancy, stretches the fluid and this enables more fluid to penetrate inside the cylinder for a constant values of Da and Re. The significance of permeability variation on drag coefficient and wake length is less than that of buoyancy variations that is considered in this study.
- The mean Nusselt number increases with the increase of Da and this increment is found to be more significant between 10^{-3} and 10^{-2} irrespective to Re and buoyancy condition. The stretched and narrow thermal field behind the porous cylinder corresponds for the reduction of thermal boundary layer at higher Da and buoyancy levels and hence, heat transfer rate is found to be maximum at this levels. At low Re, there is no significant change in heat transfer rate with Da and Ri variations.
- Finally, to quantify the mean Nusselt number at different buoyancy levels, three correlations as a function of Re and Da are obtained. Also, a common correlation that accounts the variation of Ri is formulated with correlation coefficient and maximum deviation being 0.994 and 8.77%, respectively.

From this study, it is clear that the choice of permeability value and aiding buoyancy condition plays an important role to tune the flow and heat transfer characteristics for practical applications. The heat transfer magnification is more pronounced in case of channel flow [18], cross buoyancy flow and it is expected to be more significant for a completely heated permeable square cylinder with different incident angle of flow. Hence, a detailed study on cross buoyancy heat transfer characteristics around a porous square cylinder in a confined channel with various incident angle of flow can be carried out in future.

Conflict of interest

We wish to confirm that there are no known conflicts of interest.

Acknowledgement

References

[1] D.B. Ingham, I. Pop, Transport Phenomena in Porous Media, Elsevier, UK, 1998.
[2] I. Pop, D.B. Ingham, Transport Phenomena in Porous Media II, Elsevier, UK, 2002.
[3] D. Das, S. Hassanizadeh, Upscaling Multiphase Flow in Porous Media, vol. 58, Springer, The Netherlands, 2005.
[4] D.A. Nield, A. Bejan, Convection in Porous Media, Springer Science & Business Media, New York Heidelberg Dordrecht London, 2006.
[5] P. Vadász, Emerging Topics in Heat and Mass Transfer in Porous Media: From Bioengineering and Microelectronics to Nanotechnology, vol. 22, Springer Science & Business Media, USA, 2008.
[6] M.J. De Lemos, Turbulence in Porous Media: Modeling and Applications, second ed., Elsevier, USA, 2012.
[7] K. Vafai, Handbook of Porous Media, second ed., Crc Press, Taylor & Francis Group, Boca Raton, 2015.
[8] M. Dehghan, M.S. Valipour, S. Saedodin, Temperature-dependent conductivity in forced convection of heat exchangers filled with porous media: a perturbation solution, Energy Convers. Manage. 91 (2015) 259–266.
[9] J. Ma, Y. Sun, B. Li, H. Chen, Spectral collocation method for radiative–conductive porous fin with temperature dependent properties, Energy Convers. Manage. 111 (2016) 279–288.
[10] B. Kundu, K.-S. Lee, A proper analytical analysis of annular step porous fins for determining maximum heat transfer, Energy Convers. Manage. 110 (2016) 469–480.
[11] B. Wang, Y. Hong, L. Wang, X. Fang, P. Wang, Z. Xu, Development and numerical investigation of novel gradient-porous heat sinks, Energy Convers. Manage. 106 (2015) 1370–1378.
[12] G. Kefayati, Heat transfer and entropy generation of natural convection on non-Newtonian nanofluids in a porous cavity, Powder Technol. 299 (2016) 127–149.
[13] G. Kefayati, Simulation of double diffusive natural convection and entropy generation of power-law fluids in an inclined porous cavity with Soret and Dufour effects (Part I: Study of fluid flow, heat and mass transfer), Int. J. Heat Mass Transfer 94 (2016) 539–581.
[14] X. Chen, P. Yu, S. Winoto, H.-T. Low, Numerical analysis for the flow past a porous square cylinder based on the stress-jump interfacial-conditions, Int. J. Numer. Meth. Heat Fluid Flow 18 (5) (2008) 635–655.
[15] T.-C. Jue, Numerical analysis of vortex shedding behind a porous square cylinder, Int. J. Numer. Meth. Heat Fluid Flow 14 (5) (2004) 649–663.
[16] P. Yu, Y. Zeng, T. Lee, H. Bai, H. Low, Wake structure for flow past and through a porous square cylinder, Int. J. Numer. Meth. Heat Fluid Flow 31 (2) (2010) 141–153.
[17] B. Çuhadaroğlu, O. Turan, Numerical simulation of turbulent flow around a square cylinder with uniform injection or suction and heat transfer, Numer. Heat Transfer, Part A: Appl. 55 (2) (2009) 163–184.
[18] S.-W. Perng, H.-W. Wu, R.-H. Wang, T.-C. Jue, Unsteady convection heat transfer for a porous square cylinder varying cylinder-to-channel height ratio, Int. J. Therm. Sci. 50 (10) (2011) 2006–2015.
[19] Y.-L. Yen, P.-C. Huang, C.-F. Yang, Y.-J. Chen, Numerical study of heat transfer of a porous-block-mounted heat source subjected to pulsating channel flow, Numer. Heat Transfer, Part A: Appl. 54 (4) (2008) 426–449.
[20] S.-W. Perng, H.-W. Wu, T.-C. Jue, Numerical investigation of heat transfer enhancement on a porous vortex-generator applied to a block-heated channel, Int. J. Heat Mass Transfer 55 (11–12) (2012) 3121–3137.
[21] I.V. Morenko, V.L. Fedyaev, E.R. Galimov, Cross-flow and heat transfer of porous permeable cylinder, IOP Conf. Ser.: Mater. Sci. Eng. 86 (2015) 012012.
[22] S. Chikh, A. Boumedien, K. Bouhadef, G. Lauriat, Analysis of fluid flow and heat transfer in a channel with intermittent heated porous blocks, Heat Mass Transfer 33 (5–6) (1998) 405–413.
[23] S. Rashidi, M. Bovand, I. Pop, M.S. Valipour, Numerical simulation of forced convective heat transfer past a square diamond-shaped porous cylinder, Transport Porous Media 102 (2) (2014) 207–225.
[24] G. Hwang, C. Chao, Effects of wall conduction and Darcy number on laminar mixed convection in a horizontal square porous channel, J. Heat Transfer 114 (3) (1992) 614–621.
[25] J.H. Bae, J.M. Hyun, J.W. Kim, Mixed convection in a channel with porous multiblocks under imposed thermal modulation, Numer. Heat Transfer, Part A: Appl. 46 (9) (2004) 891–908.
[26] F. Chou, C. Cheng, W. Lien, Analysis and experiment of non-Darcian convection in horizontal square packed-sphere channels-II. Mixed convection, Int. J. Heat Mass Transfer 35 (5) (1992) 1197–1207.
[27] I. Kurtbas, N. Celik, Experimental investigation of forced and mixed convection heat transfer in a foam-filled horizontal rectangular channel, Int. J. Heat Mass Transfer 52 (5) (2009) 1313–1325.
[28] H.-W. Wu, R.-H. Wang, Mixed convective heat transfer past a heated square porous cylinder in a horizontal channel with varying channel height, J. Heat Transfer 133 (2) (2011) 022503.
[29] N. Sharma, A.K. Dhiman, S. Kumar, Mixed convection flow and heat transfer across a square cylinder under the influence of aiding buoyancy at low Reynolds numbers, Int. J. Heat Mass Transfer 55 (9) (2012) 2601–2614.
[30] N. Guerroudj, H. Kahalerras, Mixed convection in a channel provided with heated porous blocks of various shapes, Energy Convers. Manage. 51 (3) (2010) 505–517.
[31] N. Guerroudj, H. Kahalerras, Mixed convection in an inclined channel with heated porous blocks, Int. J. Numer. Meth. Heat Fluid Flow 22 (7) (2012) 839–861.
[32] A.A. Mohamad, Lattice Boltzmann Method: Fundamentals and Engineering Applications with Computer Codes, Springer Science & Business Media, London Dordrecht Heidelberg New York, 2011.
[33] A. Karimipour, A.H. Nezhad, A. D'Orazio, E. Shirani, The effects of inclination angle and Prandtl number on the mixed convection in the inclined lid driven cavity using lattice Boltzmann method, J. Theor. Appl. Mech. 51 (2) (2013) 447–462.
[34] G. Kefayati, Mesoscopic simulation of double-diffusive mixed convection of Pseudoplastic Fluids in an enclosure with sinusoidal boundary conditions, Comput. Fluids 97 (2014) 94–109.
[35] G. Kefayati, Mesoscopic simulation of mixed convection on non-Newtonian nanofluids in a two sided lid-driven enclosure, Adv. Powder Technol. 26 (2) (2015) 576–588.
[36] G.R. Kefayati, FDLBM simulation of double-diffusive mixed convection of shear-thinning fluids between two-square concentric duct annuli, Heat Mass Transfer 51 (11) (2015) 1505–1521.
[37] A. Karimipour, M.H. Esfe, M.R. Safaei, D.T. Semiromi, S. Jafari, S. Kazi, Mixed convection of copper–water nanofluid in a shallow inclined lid driven cavity using the lattice Boltzmann method, Phys. A: Stat. Mech. Appl. 402 (2014) 150–168.
[38] A. Karimipour, A.H. Nezhad, A. D'Orazio, M.H. Esfe, M.R. Safaei, E. Shirani, Simulation of copper–water nanofluid in a microchannel in slip flow regime using the lattice Boltzmann method, Euro. J. Mech. - B/Fluids 49 (2015) 89–99.
[39] A. Karimipour, A.H. Nezhad, A. D'Orazio, E. Shirani, Investigation of the gravity effects on the mixed convection heat transfer in a microchannel using lattice Boltzmann method, Int. J. Therm. Sci. 54 (2012) 142–152.
[40] Z. Nikkhah, A. Karimipour, M.R. Safaei, P. Forghani-Tehrani, M. Goodarzi, M. Dahari, S. Wongwises, Forced convective heat transfer of water/functionalized multi-walled carbon nanotube nanofluids in a microchannel with oscillating heat flux and slip boundary condition, Int. Commun. Heat Mass Transfer 68 (2015) 69–77.
[41] A. Karimipour, New correlation for Nusselt number of nanofluid with Ag/Al$_2$O$_3$/Cu nanoparticles in a microchannel considering slip velocity and temperature jump by using lattice Boltzmann method, Int. J. Therm. Sci. 91 (2015) 146–156.
[42] M. Breuer, J. Bernsdorf, T. Zeiser, F. Durst, Accurate computations of the laminar flow past a square cylinder based on two different methods: lattice-Boltzmann and finite-volume, Int. J. Heat Fluid Flow 21 (2) (2000) 186–196.
[43] V. Babu, A. Narasimhan, Investigation of vortex shedding behind a porous square cylinder using lattice Boltzmann method, Phys. Fluids 22 (5) (2010) 053605 (1994-present).
[44] Q. Liu, Y.-L. He, Q. Li, W.-Q. Tao, A multiple-relaxation-time lattice Boltzmann model for convection heat transfer in porous media, Int. J. Heat Mass transfer 73 (2014) 761–775.
[45] Z. Guo, T. Zhao, Lattice Boltzmann model for incompressible flows through porous media, Phys. Rev. E 66 (3) (2002) 036304.
[46] C.-Y. Zhao, L. Dai, G. Tang, Z. Qu, Z. Li, Numerical study of natural convection in porous media (metals) using Lattice Boltzmann Method (LBM), Int. J. Heat Fluid Flow 31 (5) (2010) 925–934.
[47] Z. Guo, T. Zhao, A lattice Boltzmann model for convection heat transfer in porous media, Numer. Heat Transfer, Part B 47 (2) (2005) 157–177.
[48] T. Seta, E. Takegoshi, K. Okui, Lattice Boltzmann simulation of natural convection in porous media, Math. Comput. Simul. 72 (2) (2006) 195–200.

[49] P.A.K. Lam, K.A. Prakash, A numerical investigation of heat transfer and entropy generation during jet impingement cooling of protruding heat sources without and with porous medium, Energy Convers. Manage. 89 (2015) 626–643.

[50] W. Minkowycz, A. Haji-Sheikh, K. Vafai, On departure from local thermal equilibrium in porous media due to a rapidly changing heat source: the Sparrow number, Int. J. Heat Mass Transfer 42 (18) (1999) 3373–3385.

[51] S. Dhinakaran, J. Ponmozhi, Heat transfer from a permeable square cylinder to a flowing fluid, Energy Convers. Manage. 52 (5) (2011) 2170–2182.

[52] W.-S. Fu, H.-C. Huang, W.-Y. Liou, Thermal enhancement in laminar channel flow with a porous block, Int. J. Heat Mass Transfer 39 (10) (1996) 2165–2175.

[53] Q. Zou, X. He, On pressure and velocity boundary conditions for the lattice Boltzmann BGK model, Phys. Fluids 9 (6) (1997) 1591–1598 (1994-present).

[54] Y. Zhang, R. Qin, Y. Sun, R.W. Barber, D. Emerson, Gas flow in microchannels–a lattice Boltzmann method approach, J. Stat. Phys. 121 (1–2) (2005) 257–267.

[55] P.D. Noymer, L.R. Glicksman, A. Devendran, Drag on a permeable cylinder in steady flow at moderate Reynolds numbers, Chem. Eng. Sci. 53 (16) (1998) 2859–2869.

[56] X. He, L.-S. Luo, Theory of the lattice Boltzmann method: from the Boltzmann equation to the lattice Boltzmann equation, Phys. Rev. E 56 (6) (1997) 6811.

[57] A. Artoli, A. Hoekstra, P. Sloot, 3D pulsatile flow with the lattice Boltzmann BGK method, Int. J. Modern Phys. C 13 (08) (2002) 1119–1134.

[58] A. Artoli, A. Hoekstra, P. Sloot, Accelerated Lattice BGK method for unsteady simulations through Mach number annealing, Int. J. Modern Phys. C 14 (06) (2003) 835–845.

[59] A. Sharma, V. Eswaran, Heat and fluid flow across a square cylinder in the two-dimensional laminar flow regime, Numer. Heat Transfer, Part A: Appl. 45 (3) (2004) 247–269.

[60] B. Paliwal, A. Sharma, R. Chhabra, V. Eswaran, Power law fluid flow past a square cylinder: momentum and heat transfer characteristics, Chem. Eng. Sci. 58 (23) (2003) 5315–5329.

[61] D. Yu, R. Mei, L.-S. Luo, W. Shyy, Viscous flow computations with the method of lattice Boltzmann equation, Prog. Aerospace Sci. 39 (5) (2003) 329–367.